

A closer look at corrosion of steel reinforcement bars in concrete using 3D neutron and X-ray computed tomography

Samanta Robuschi^{a,*}, Alessandro Tengattini^{b,c}, Jelke Dijkstra^a, Ignasi Fernandez^a, Karin Lundgren^a

^a Chalmers University of Technology, Göteborg, Sweden

^b Université Grenoble Alpes, Grenoble, France

^c Institut Laue-Langevin, 71 avenue des Martyrs, CS 20156, 38042 Grenoble cedex 9, France

ARTICLE INFO

Keywords:

3D neutron and X-ray computed tomography
Corrosion
Reinforced concrete

ABSTRACT

Corrosion of reinforcing bars constitutes the largest threat to the durability of concrete structures. Thus, several studies have investigated the nature of the corrosion products, most using post-mortem analyses. However, corrosion products evolve when in contact with oxygen, hindering result interpretation. This work presents instead a state-of-the-art, non-destructive 3D method for the assessment of corrosion of embedded reinforcements.

Multimodal neutron and X-ray tomography was used to observe, non-destructively, the characteristics of the corrosion products in two concrete samples, with the aim of investigating possible benefits of the use of this technique for reinforced concrete structures. One sample was naturally corroded, extracted from an 81-year-old bridge, the other was corroded via the galvanostatic method, resulting in corrosion-induced cracks. Quantitative and qualitative data was acquired, including the iron-to-rust volumetric ratio in macroscopic interfacial voids and the thickness of the corrosion layer at the steel concrete interface. The iron-to-rust volumetric ratio corresponded to large, soluble, corrosion products, forming in environments with low availability of oxygen for both samples.

1. Introduction

Corrosion of the reinforcing bars is known to be the most common cause of deterioration of reinforced concrete (RC) structures [1]. The corrosion process initiates with the depassivation of the reinforcing bar, most commonly due to contact with chlorides or carbon dioxide. Once the reinforcing bar is depassivated, corrosion products are generated as a result of the reaction of iron molecules with oxygen and hydrogen.

Corrosion products occupy a larger volume than the steel they originate from. Consequently, the volume expansion from increasing presence of corrosion products results in increasing radial pressure applied at the steel/concrete interface, eventually leading to cracking and spalling of the concrete cover [2]. Simultaneously, corrosion results in a loss of cross sectional area of the reinforcing bar, thus reducing its strength and ductility [3,4]. Hence, the corrosion process impairs the structural behaviour, and therefore the safety of RC structures [5–7]. It follows that accurate predictions of the corrosion damages are fundamental for the safety assessment of infrastructure currently in use and to

improve future designs.

Recently, a number of models have been developed to describe the various stages of the corrosion process, from initiation to propagation [8–10], and to assess their impact on the structural behaviour of RC structures. Comprehensive predictive models for the structural effects of degradation due to corrosion, however, rely on the knowledge of a large number of parameters, some of which are difficult to measure and, in some cases, controversial [11,12]. This study proposes the use of neutron and X-Ray tomography as a way to acquire further, necessary, knowledge on those parameters necessary to predict the structural consequences of corrosion damages in RC structures. The parameters that have been considered in this study are presented below.

1.1. Iron-to-rust ratio

A first, fundamental parameter for describing the corrosion process is the iron-to-rust ratio. The iron-to-rust ratio describes the volumetric expansion of the corrosion products, and it is particularly important for

* Corresponding author.

E-mail address: samanta.robuschi@chalmers.se (S. Robuschi).

the modelling of corrosion-induced concrete cracking. It is known to vary between 2.2 and 6.4 depending on the availability of oxygen and hydrogen at the time of formation of the corrosion products [13,14]. Fig. 1 summarises different oxides and hydroxides generated in the corrosion process and the corresponding iron-to-rust volume ratio.

In most of the predictive models currently in use for corrosion-related cracking [8–10,15–17] this iron-to-rust ratio is assumed to be constant. The ratio is either derived indirectly from a calibration of laboratory experiments at boundary level, or based on the expected chemical composition of the corrosion products, and generally results in values varying between 2 and 4. The composition of rust, however, is expected to change with exposure to different environmental conditions [18,19], and corrosion mechanisms [20]. Hence, the use of a fixed ratio for modelling the expansion of the corrosion products is unsuitable for capturing different scenarios.

This variability is corroborated, for example, by the tests of Syed [19], where X-ray diffraction was used to identify different corrosion products formed on hot and cold rolled carbon steel after 3 years of exposure to different environments. The samples exhibited large differences in mass loss and composition of the resulting products. Zhao et al. [18] also used X-ray diffraction, together with thermal analysis, to evaluate the rust expansion coefficient of 8 samples exposed to different chloride environments, and concluded that humidity and oxygen supply are the main factors governing the magnitude of the expansion coefficient of the corrosion products.

Most experimental methods for the study of the corrosion process of reinforcing bars embedded in concrete require the destruction of the investigated sample, followed by the manual extraction of the corrosion products for later analysis. This process can introduce a considerable error in the study, if corrosion products are exposed to oxygen, since it would change their chemical composition [21]. This, in turn, affects the volume occupied by the corrosion products. Additionally, mechanical interaction, such as cutting or breaking the sample, inevitably disturbs the distribution of the corrosion products. Most of these analyses are also not spatially resolved, and can only provide bulk-averaged information about the corrosion process, which cannot shed light on its spatial distribution and on its interrelation with the development of fracture networks. An additional limitation of the traditional *post-mortem* analyses is that they are generally limited to a single point in time and it is therefore impossible to study the progressive growth of the corrosion products and the related damage.

In this work, we propose the use of novel non-destructive tools,

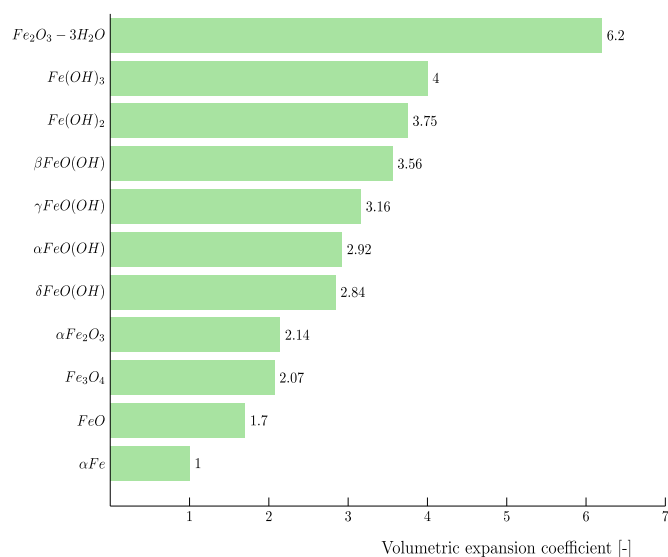


Fig. 1. Relative iron to rust volume for different iron oxides and hydroxides [13,14].

which provide 3D, quantitative information about the corrosion processes, specifically the volume loss of steel and the corresponding iron-to-rust-ratio. Besides the reduced risk of altering the studied processes, the non-destructive nature of the approach also opens new venues in the time-resolved studies of the inception and development of corrosion products, which is pivotal in understanding its close relationship with the formation of fractures.

1.2. Corrosion Accommodating Region

Recent corrosion models commonly assume the presence of a “porous zone” [22,8]. This region, adjacent to the reinforcement bar, is able to accommodate corrosion products without inducing additional stresses on the concrete matrix, thus delaying the formation of corrosion-induced cracks. The more concise term Corrosion Accommodating Region (CAR) [23] will be used in this work instead of porous zone, since concrete is a porous material. The CAR is known to be an important parameter for the accurate prediction of corrosion induced-cracking, and has been the object of extensive research. However, there is no general agreement on its properties.

Petre-Lazar [24] was among the firsts to suggest that the rust fills up the pores close to the reinforcement bar before starting to increase the stresses in the structure. This early intuition was supported by scratching tests to assess the mechanical properties of the corrosion products revealing that rust is a cohesionless assemblage of incompressible crystals. The CAR was first introduced in numerical modelling by Liu and Weyers [25], after observing significant delay between the prediction of corrosion-induced cracks in previous corrosion models and the cracking time registered in experiments. They proposed a zone described by a uniform 12.5 μm thick layer surrounding the bar.

The thicknesses of the CAR are typically assumed to be in the range of 10–20 μm , although more extreme values are also adopted by some authors (between 2 μm and 180 μm) [26]. This variability strongly indicates a need for further investigations, suggesting that the use of the CAR might in some cases become a mere fitting parameter for corrosion models [26].

A first attempt to use non destructive methods to study the CAR thickness was carried out by Michel et al. [23,27]. In these works, the average concentration of corrosion products at different distances from the bar surface was quantified using the variation in X-ray attenuation measured in radiographs. The corrosion product was assumed to correspond to Fe_2O_3 , and the analysed samples were artificially corroded. The CAR was observed to increase in size with time, reaching 0.22 mm thickness at the time of cracking. This phenomenon was probably due to the opening of micro-cracks, connecting additional concrete pores. In the work of Michel et al. [27], a conceptual model was developed to describe the penetration of corrosion products in the cementitious material, where a uniform CAR was defined around the reinforcing bar. Though the model showed good agreement with the experimental data, X-ray attenuation measurements showed that the penetration of the corrosion products was non-uniform. This affected the ability of the model to accurately predict deformations at the steel-concrete interface and time to corrosion-induced cracking.

Corrosion-induced cracking results in increased availability of space for the corrosion products to expand, and possibly even reach the external surface of the concrete through the cracks. To describe this phenomenon, Michel et al. [27] proposed a CAR model divided in two parts: one, directly in contact with the bar, representing the intrinsic porosity of concrete, and a second, larger layer, created by the opening of corrosion-induced micro-cracks around this porous zone. However, according to experimental data from Wong et al. [28], after corrosion-induced cracking initiates, corrosion products preferentially deposit in the resulting macro-cracks rather than in the pores. This implies that the opening of micro-cracks, and the resulting interconnection of additional pores in the surrounding of the bar, is less consequential to the corrosion propagation, and can be assumed to be negligible in the modelling of the

CAR.

In this work, an attempt to quantify the thickness of the corrosion products, and of the voids, at the steel/concrete interface is presented. It should be noted that this is not exactly equivalent to the thickness of the CAR; especially for one of the analysed samples which had corrosion-induced cracks, they are not expected to agree. Nevertheless, the thickness of the corrosion products is an important measure that can be used for calibration at modelling.

1.3. Migration of corrosion products through cracks

Another topic of interest in this work is the effect of corrosion-induced cracks on the distribution of the corrosion products surrounding the reinforcing bar. Various forms of corrosion products migration through corrosion-induced cracks are implemented in models reported in literature, e.g., [9,29]. Fahy et al. [29] modelled the transport of corrosion products through cracks as a function of the pressure built up due to the structural confinement of the corrosion products, i.e., the corrosion products migrates through concrete driven by a gradient in fluid pressure resulting from the structural confinement of the reinforcing bar in the concrete matrix. However, there is no general agreement on the migration mechanism of the corrosion products and specifically on the influence of pores and corrosion-induced micro- and macro-cracks.

1.4. X-ray and neutron tomography

In this work, multimodal X-ray and neutron tomography is adopted to investigate the properties and spatial distribution of the corrosion products, in 3D and non destructively, for two corroded concrete samples, taking advantage of the high complementarity of these techniques. The high hydrogen-sensitivity of neutron imaging allows in fact to easily discern the hydrogen-rich cement paste from the quartzitic aggregates and the pores. Pores and aggregates are almost neutron transparent and are therefore hard to discern from one another. Most importantly, the high hydrogen content of the corrosion products makes neutron imaging a promising technique for the study of the spatial distribution of corrosion products within the sample. In contrast, the attenuation in X-ray is a function of material density and the atomic number of the components of the sample. It follows that pores and fractures can be easily identified, allowing, together with neutron imaging, to gather a complete description of the constituents of the sample.

Scans on each sample are acquired with both techniques, and registered onto each other using an alignment procedure based on the geometrical features of the specimens. The multimodal registration allows an improved quantification of the phases present in the sample, by taking advantage of the different sensitivities of the two methods. Few attempts have been carried out to utilise these techniques for concrete samples. Stamati et al. [30] used both neutron and X-ray tomography to successfully separate each phase of the concrete meso-structure. Roubin et al. [31] applied the algorithm for multimodal registration developed in [32] to a concrete sample, and successfully identified its different phases. Dauti et al. used neutron tomography on concrete samples subjected to high-temperature to assess moisture distribution [33] and to gain insights on commonplace experimental procedures employed for the study of concrete behaviour [34]. In a technical note by Zhang et al. [35], neutron tomography images of a pre-cracked reinforced concrete sample subjected to wetting and drying cycles were obtained at a neutron spallation source. The 3D visualisation and the cross section images obtained show the potential of such technique of identifying reinforcement corrosion. However, they do not present any further quantification attempt. Šavija et al. and Rossi et al. [36,37] used X-ray computed tomography (X-ray CT) to observe the distribution of corrosion products in artificially and naturally corroded RC specimens. Both works show the feasibility of using X-ray CT to distinguish different phases inside the concrete samples, including the presence of corrosion

products. It was not possible to distinguish between aggregates and cement paste, and the beam-hardening effect was shown to decrease the quality of the data at the steel-concrete interface. Distinguishing between aggregates and cement paste is however possible with X-ray tomography, employing advanced image processing methods, as shown by Stamati et al. [30]. The work by Rossi et al. shows corrosion pits prevalently forming in the proximity of interfacial air voids, stressing their relevance for the prediction of corrosion initiation.

The aim of this study is to investigate the potential of the combined use of neutron and X-ray tomography for observing, non-destructively, the characteristics of the corrosion products in reinforced concrete structures. The focus is on those parameters needed in analytical or numerical models of the corrosion process, such as the iron-to-rust ratio and the porosity of the concrete at the interface with the steel bar. Additionally, this study looks at the difference in dimension and distribution between corrosion products resulting from natural and galvanostatic corrosion.

The study comprises a naturally corroded and an artificially corroded RC sample. The naturally corroded sample was obtained from a decommissioned 81-year-old bridge, while the artificially corroded specimen was prepared in laboratory and artificially corroded *via* the galvanostatic method. The obtained images allowed for the identification of the different material phases of the samples, including the presence of corrosion products. The distribution of corrosion products was observed at the steel/concrete interface, around the bar, and with respect to the presence of pores. The iron-to-rust ratio was determined for those areas where corrosion products were observed to be free to expand (macro-pores). Quantitative measures of the corrosion level of the bar, and of the thickness of voids and corrosion products at the steel concrete interface are as well given.

2. Samples and methodology

The data used in the present study was acquired at the NeXT-Grenoble instrument [38] at the Institut Laue-Langevin (ILL). The two samples of this study are presented in Fig. 2.

2.1. Samples

2.1.1. Naturally corroded sample

The naturally corroded sample was a cylindrical core, with a height of approximately 81 mm, and a 25 mm diameter. A 16 mm diameter plain reinforcing bar was embedded near the centre. The sample was drilled using a water-cooled drill in September 2018, and by keeping the speed of the cutting to a minimum to avoid damaging the specimen. The sample was cored from a decommissioned bridge, located in the Swedish town of Gullspång. The bridge was built in 1935, and it was demolished in 2016 because of the heavy corrosion damage. Segments of the edge beams were analysed and tested in a connected study, where the bond between the plain reinforcing bars and the concrete was tested to assess its relationship with the presence of corrosion damage [39,40]. The compressive strength of the concrete was found to be 45.6 MPa, with a standard deviation of 4.6 MPa. The tensile strength of the steel was measured in 27 tensile tests of uncorroded bars. The average yield stress was 259.6 MPa with a standard deviation of 10.1 MPa.

The edge beams were cast by tamping the concrete, as common at the time of construction, instead of vibrating, and were exposed to natural weather conditions for 81 years, including wetting/drying, and freezing/thawing cycles, as well as de-icing salt. The original position of the core in the edge beams is shown in Fig. 3. The reinforcing bar was top-cast in the original cross section: since the size of settlements and bleeding zones increases with the height of the concrete below the reinforcing bar, macro-pores and bleeding zones are more likely to be present under horizontal top-cast bars [41,42]. According to Angst et al. [11], the corrosion initiation process may be linked to the presence of macro-pores, and may result in different distributions of pitting



Fig. 2. Samples included in the study, after coring. To the left, naturally corroded sample cored from a decommissioned bridge; to the right, artificially corroded sample with corrosion induced cracks.

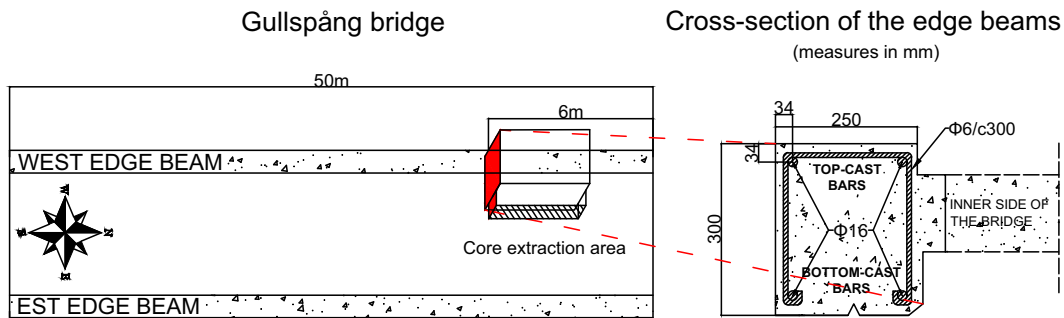


Fig. 3. Original position of the sample cored from Gullspång bridge. On the left, a view of Gullspång bridge where the position of the cored sample is marked. On the right, the nominal cross-section of the edge beams. Note that the drawings are not in the same scale.

corrosion depending on the moisture content of the pores. Differences in concrete density and pores presence in the surrounding of the bar were clearly observed in the sample. However, the original orientation of the sample was not documented at the time of cutting. The position of the bleeding zone, and consequently the bar orientation, was therefore deduced from the observed non-homogeneity in the concrete matrix.

2.1.2. Artificially corroded sample

The artificially corroded sample was prepared in the laboratory adopting a plain reinforcing bar with a nominal diameter of 16 mm extracted from the edge beams of Gullspång bridge, for consistency with the natural sample. The bar was sandblasted before casting, to remove concrete debris resulting from the extraction process and possible traces of corrosion products on its surface. A portable 3D scanner was used to acquire the 3D geometry of the bar. This allowed for a better evaluation of the steel volumetric loss linked to the corrosion process [40]. The bar was positioned in the middle of a 130×150 mm concrete cylinder. The bar was embedded in the concrete cylinder for a length of 80, while plastic holders (25 mm each) were used to cover the top and bottom parts of the bar. The cylinder was cast standing on its base in November 2018, with the reinforcing bar (which had a total length of approximately 200 mm) protruding from the top. This means that the artificially and naturally corroded samples are cast in two different directions, and it is likely to result in differences in the distribution of macro-pores at the steel-concrete interface.

The concrete was produced with natural aggregates: 943 kg m^{-3} of 0/4 natural sand and 911 kg m^{-3} of 4/16 gravel. The quantity of cement in the mix was 365 kg m^{-3} of CEM I 42.5 N (SS-EN197-1: 2011 [43]) with a water to cement ratio of 0.47, which is adequate for aggressive

environments. To achieve acceptable workability, the composition included 1% of cement weight in superplasticizer (Glenium 5118). The consistency of the resulting concrete was fluid without segregation. The compressive strength of the concrete was 47.0 MPa at 7 days and 59.5 MPa at 28 days. The concrete used was mixed with sodium chloride NaCl (4% of the concrete weight) to prevent the passivation of the reinforcing bar.

After 28 days from casting, the corrosion process was initiated by submerging half of the height of the cylinder in a solution of water and sodium chloride (5%). Corrosion was induced via the galvanostatic method, applying a constant current density of $100 \mu\text{A cm}^{-2}$ to the bar for a total of 31 days. The artificial corrosion was induced using the same test set-up as in [44], where additional information on the set-up configuration can be found. At the end of this period, the sample showed cracks on its surface, as shown in Fig. 4. Finally, in September 2019, a 31 mm core centred around the reinforcement bar was extracted from this larger cylinder, by water coring. Reducing the size of the sample was needed to increase the resolution of the acquired image data, particularly at the steel/concrete interface.

The followed procedure is a trade-off between obtaining samples that are comparable to the natural corroded sample and their suitability for subsequent neutron imaging. The use of NaCl allows for reaching reasonable corrosion levels in a short period of time by introducing chlorides in the pore solution, and therefore preventing the passivation of the reinforcement bar. However, the chlorine is highly opaque to neutrons, having a value of the absorption coefficient in between the ones of hydrogen and iron. Therefore, the presence of chlorides in the cement paste may increase its attenuation value, making it harder to distinguish between corrosion products and cement paste. The followed

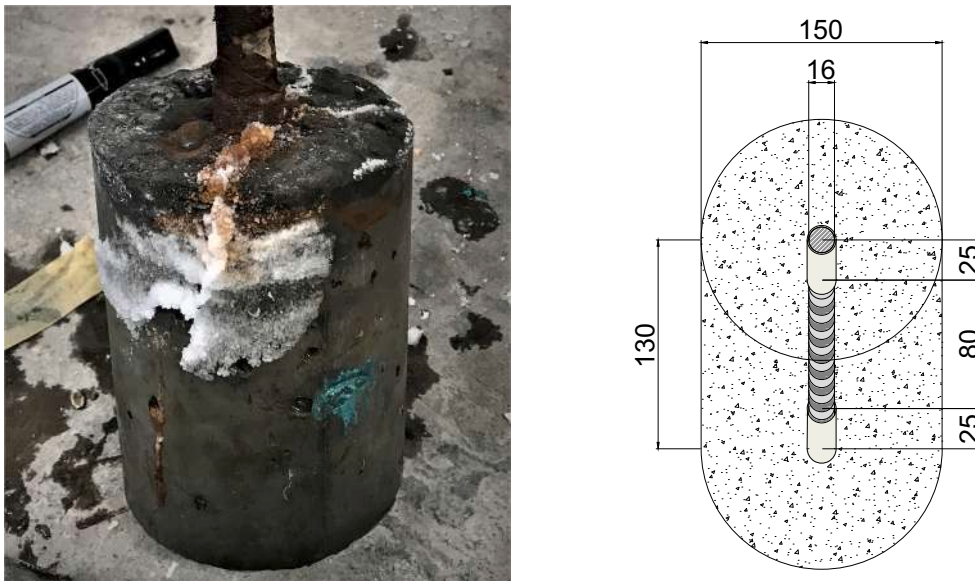


Fig. 4. On the left, artificially corroded sample, before coring. Cracks and corrosion stains are clearly visible on the surface. On the right, the geometry of the artificial sample is shown. All measures in mm.

procedure for artificial corrosion is nonetheless a common practice in corrosion studies on reinforced concrete [45]. The use of real-size components also affects the X-ray imaging, given that the large diameter of the metal reinforcement bar is highly attenuating to the X-rays. This was partially compensated by the use of relatively hard (high energy) X-ray, as detailed below.

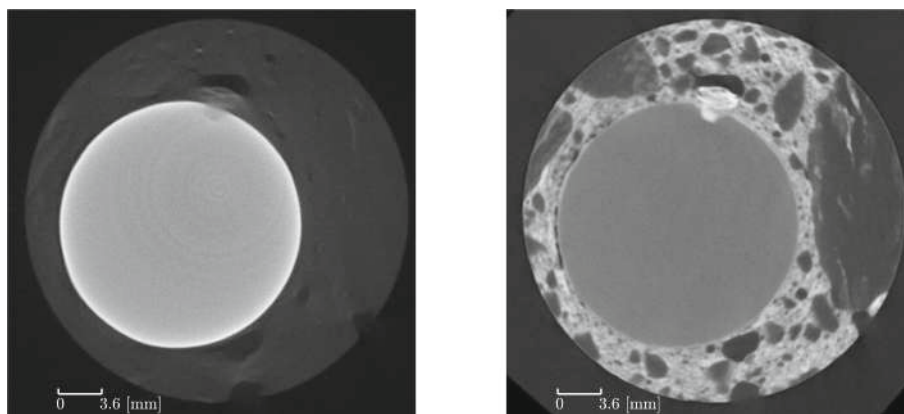
2.2. Multimodal X-ray and neutron tomography

As aforementioned, the NeXT neutron imaging beamline at Institut Laue-Langevin was used for acquiring the neutron and X-ray tomographies of the concrete specimens. The instrument combines neutron imaging capabilities with a conic X-ray source/detector pair perpendicular to the path of the neutrons [38]. This allows performing both image acquisition in the same experimental set-up, one after the other.

The multimodal imaging takes advantage of the high complementarity in the attenuation mechanisms that neutron and X-rays have when interacting with specimens. In X-ray tomography, the attenuation coefficient of an element increases with the density and atomic number of the element, *i.e.*, hydrogen is very transparent, while iron is strongly

attenuated. In contrast, the attenuation of the neutron beam does not increase monotonically with the atomic number of the element. For example, hydrogen has a very high coefficient of attenuation, while the neutron attenuation of iron is seventeen times lower, if normalised by density.

This is reflected in Fig. 5, which shows a cross-section from the naturally corroded sample, as captured with X-ray (left) and neutron imaging (right), after the two data sets were aligned. In the X-ray image, the low density pores are easily recognisable but aggregates and the cement paste, having similar densities, are hard to distinguish. In the neutron image, conversely, the cement paste has higher attenuation than quartzitic aggregates, due to the presence of both free and chemically bound water. Nonetheless, pores and voids are hard to distinguish from the aggregates, which can be compensated with the X-ray data. Most importantly, the high hydrogen content of corrosion products makes their presence highly visible, which is key in the present study. Conversely the more commonplace X-rays have difficulties in the presence of the relatively large reinforcing bar (16 mm in diameter), in particular on the boundary between the steel and the concrete (the beam hardening effect highlighted by the large gradient in X-ray attenuation



A: X-ray tomography

B: Neutron tomography

Fig. 5. On the left, a view of a cross section with a corrosion pit from the naturally corroded sample obtained with X-ray tomography. On the right, view of the corresponding cross section after alignment, as obtained with neutron imaging. The highest coefficients of attenuation are in white.

fields inside the reinforcement bar).

2.3. Data acquisition and post processing

2.3.1. Data acquisition

For each of the two samples, neutron and X-ray tomographies were acquired. The pixel size was of $26 \mu\text{m px}^{-1}$ for the neutron images, and $36 \mu\text{m px}^{-1}$ for the X-ray, as summarised in Table 1. The resolution allowed for the observation of the composition of the samples, and the corrosion distribution.

The data from this study included, however, different sources of noise which made it more challenging to identify all the constituents. The main source of noise in the neutron data for the naturally corroded sample stems from the presence of scandium (Sc) in the cement paste, which was revealed by a neutron spectroscopy of the sample. The element, classified as a rare-earth material, is rarely present in concrete, but has a high adsorption coefficient in neutron imaging, similar to that of hydrogen. Additionally, one of the isotopes of scandium has a half-life of 83.8 days. This introduced additional problems with handling of the sample after the acquisition of the images.

The artificially corroded sample also contained elements that decreased the quality of the data on the corrosion distribution: in addition to the aforementioned presence of sodium chloride, the sample was also humid at the time of scanning. To decrease the interference produced by large amounts of water in the cement paste, the sample was dried at 85°C for 3 h prior to scanning.

2.3.2. Reconstruction of the data

These sets of radiographies were reconstructed into the corresponding 3D volumes by means of the Feldkamp (FDK) back projection algorithm, as implemented in the commercial software X-act (from RX-Solutions).

2.3.3. Multimodal registration

Post-processing of the reconstructed images was mainly carried out with a combination of MATLAB® [46] and ImageJ [47,48]. Post-processing aimed at matching data acquired from neutron and X-ray tomography. Multimodal registration aligns the two types of images, obtained from the same sample, onto each other. This is done by moving the two obtained 3D attenuation fields (X-ray and neutron) in the 3D space. This requires for the scans to have similar resolutions (a negligible rounding error may affect the final pixel size). Hence, the neutron data was rescaled to a lower theoretical pixel resolution of $36 \mu\text{m}$ to match the X-ray data. This multimodal registration is essential to take full advantage of the multimodal nature of the information to identify the phases, which in turn improves subsequent quantitative analysis.

The method used for multimodal registration makes use of the particular geometrical properties of the samples, and notably their cylindrical shape, the presence of a plain reinforcing bar and defects (voids) in the external perimeter of the sample. The post-processing process is summarised in detail in Appendix A.

The outcome of the multimodal registration is the realigned neutron

Table 1
Neutron and X-ray tomography acquisition data.

	Type of image acquisition	
	Neutron tomography	X-ray tomography
Expected resolution [μm]	32	45
Theoretical voxel size [$\mu\text{m px}^{-1}$]	26	36
Number of projections	1300	1300
Total exposure time [min]	178	30
Exposure time (neutron source) [s]	2.75	–
Field of view (neutron source) [cm]	6.5	–
Frame rate per second [s^{-1}]	–	5
Voltage (X-ray source) [kW]	–	214
Current (X-ray source) [μA]	–	140

data. An example of the results is shown in Fig. 6, where a horizontal cross-section of each 3D data set is presented. The new aligned data was subsequently used to divide the image in different phases, corresponding to background, cement paste, aggregates, voids, reinforcing bar and corrosion products as detailed in the next section.

2.3.4. Phase segmentation

After multimodal registration, the tomographies were divided into different material phases, a process generally referred to as segmentation. Several approaches exist in literature, one of the more common classes of which relies on classifying the voxels constituting the image based on the reconstructed attenuation values. Thresholding was applied to divide the sample into its constituents, now characterised by discernible attenuation coefficients. Thresholding was performed using Multi Otsu's method [49] on the combined neutron and X-ray data. The different components of the sample were identified iteratively, taking advantage of the alignment between the data.

The occurrence of a given couple of attenuation values in X-rays and neutrons for each voxel can then be employed to identify the phases. For example, pores are characterised by a low X-ray and neutron attenuation, while aggregates have high X-ray and low neutron attenuation. This approach was used to identify the key components. Initially, the histogram describing the distribution of the attenuation coefficients in the X-ray data was used to divide the concrete sample from its background. The histogram resulting from the superimposed data was used to identify the reinforcing bar, and the histogram of the attenuation coefficients in the neutron data was used to identify the aggregates. Once these three components were identified, a new set of data was generated, where the three defined phases were removed from the sample (*i.e.* set to be equal to zero). Thresholding was then used again to define the remaining components from the histogram of the superimposed data (voids, corrosion products and cement paste).

An example of the final result is shown in Fig. 7. It should be observed that the theoretical voxel size of the sample ($36 \mu\text{m}$) did not allow for distinguishing either micro-pores or the interfacial transition zone (ITZ), their size being smaller than the theoretical voxel size.

2.3.5. Thickness of the corrosion and voids layer surrounding the bar

Once the samples have been subdivided into phases, the thickness of the porous region and of the corrosion products surrounding the bar can be evaluated. Measurements were performed on the individual slices.

For each slide, the reinforcing bar was first isolated thanks to the segmentation detailed above, and its perimeter and centre were identified. Then, each slide was divided into 720 radial sectors (*i.e.*, 0.5° increments), selecting as origin the centre of the reinforcing bar. Within these radial sectors, a subregion delimited by the external perimeter of the bar on one side, and by the background on the other, was then used to study the composition, and notably the amount of voids and of corrosion products for that angle. For each radial sector, the maximum distance between the external perimeter of the bar and the corrosion product/voids in the sector was then computed.

The thickness of the corrosion product/voids was defined as a continuous layer of the phase surrounding the bar. To account for the presence of noise in the measurements, a maximum discontinuity (*i.e.*, the presence of a phase not identified as corrosion products/voids inside the layer) equal to 2 pixels in the thickness was allowed in the computation.

2.3.6. Evaluation of the expansion coefficient

The iron-to-rust volumetric ratio of the corrosion products was evaluated in those areas where corrosion products were assumed to be free to expand, *i.e.*, interfacial macroscopic voids where corrosion pits had formed. A number of corrosion pits were individually selected based on whether they satisfied the following conditions:

- Corrosion products were present in the pore;

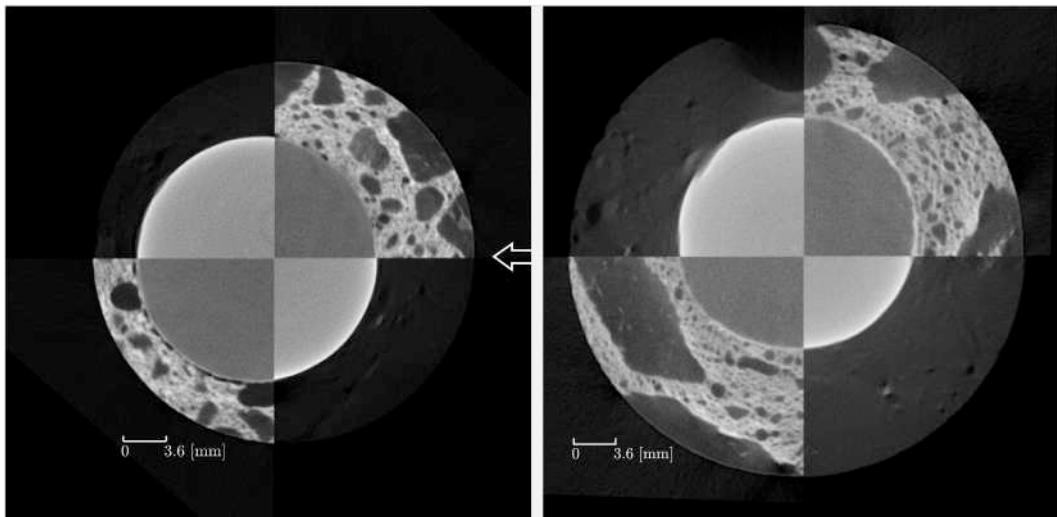


Fig. 6. Example of the realigned data-set. Cross sections of the naturally corroded sample (left) and the artificially corroded sample (right) are shown. A white arrow marks the expected casting direction in the naturally corroded sample.

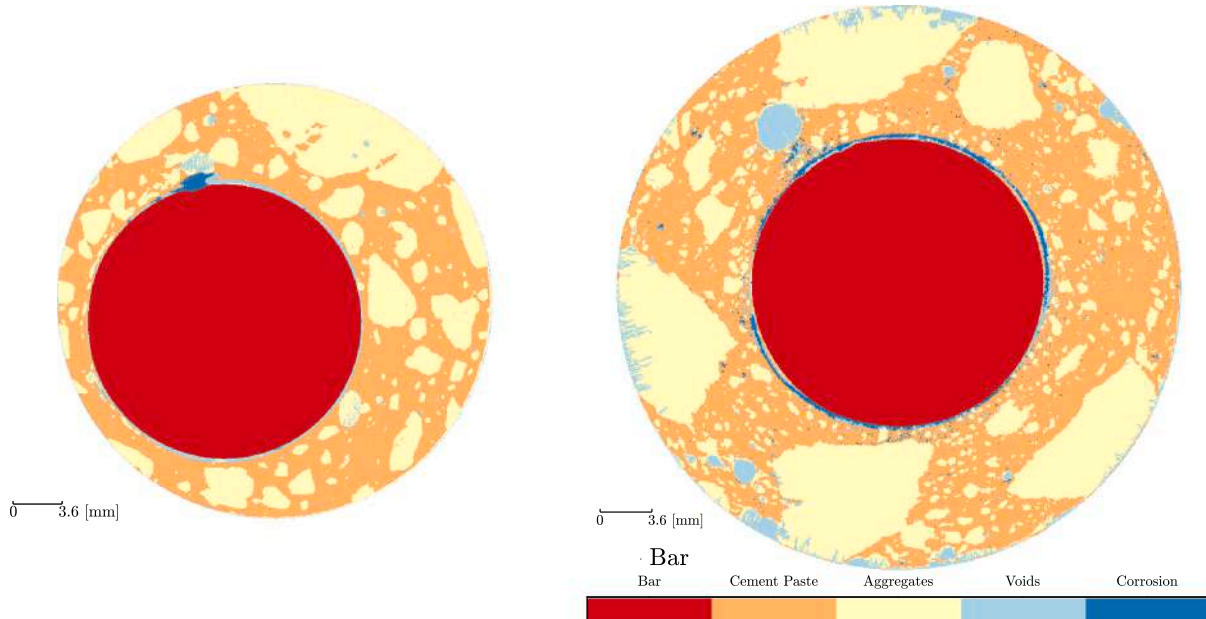


Fig. 7. Phase segmentation of the samples. Cross sections of the naturally corroded sample (left) and the artificially corroded sample (right) are shown.

- The macroscopic pore was not filled with corrosion products, so that corrosion products were likely not compressed;
- No external cracks were connected to the pore, which would have allowed part of the corrosion products to migrate outside the specimen.

A total of three pores satisfying these conditions were observed in the samples, of which two were found in the naturally corroded sample and one in the artificially corroded sample (see Fig. 8).

The procedure for the evaluation of the expansion coefficients consisted first in isolating the volume of interest, *i.e.* the pore and the corresponding corroded bar surface (see Fig. 8). Then, the total volume of the corrosion products was calculated starting from the previously isolated corrosion phase.

The total loss of steel was calculated by assuming the following:

- For the naturally corroded sample, the average uncorroded area is assumed to be equal to 203.02 mm^2 , as obtained from 3D scanning of bars from the same edge beams in a previous study [39];
- For the artificially corroded sample, the geometry of the reinforcing bar was evaluated before casting, and therefore the average uncorroded area was known and equal to 207.92 mm^2 ;
- The loss of steel was equal to the difference between the measured local volume of the bar, and the volume of a perfectly circular bar, centred in the centre of the reinforcing bar and having an area equal to the uncorroded area. The theoretical radius was based on the average uncorroded area. Note that the volumetric difference was evaluated only in the subvolume of interest of the pit, calculated from the theoretical steel area in the marked region in Fig. 8.

2.3.7. Evaluation of the corrosion level

Finally, the corrosion level of the reinforcing bars was evaluated, where the corrosion level was defined as the loss of cross sectional area

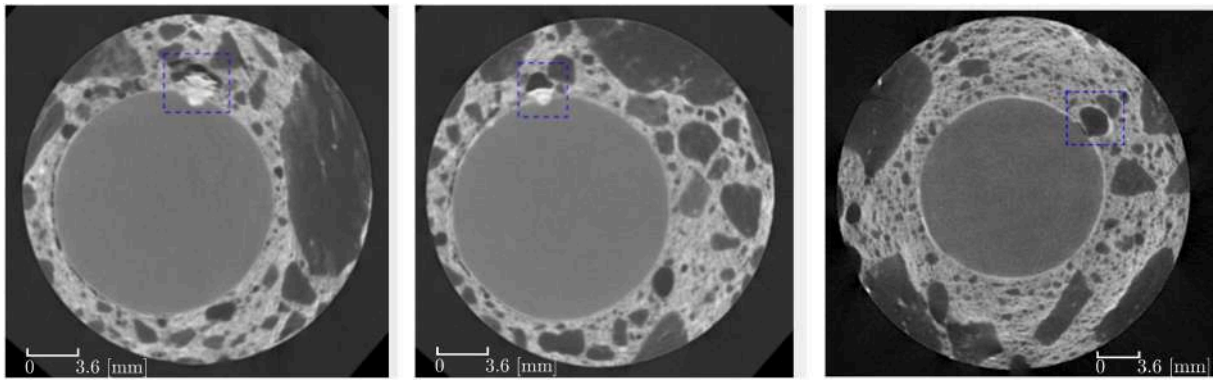


Fig. 8. Cross sectional view of the corrosion pits used for the computation of the iron-to-rust ratio (as captured with neutron imaging). Two pits were found in the naturally corroded sample (left and centre), one in the artificially corroded sample (right). In blue, the area of the cross-section considered for the evaluation of the expansion coefficient. (For interpretation of the references to colour in this figure legend, the reader is referred to the web version of this article.)

of the bar along its length. The corrosion level along the length of the bar (C_i) was evaluated based on the ratio between the area of the reinforcing bar, as obtained from each cross sectional slice through phase segmentation (A_i), and the average area of the uncorroded bar (A_m), see Section 2.3.6:

$$C_i = 1 - \frac{A_i}{A_m} \quad (1)$$

3. Results and discussion

The results of this study are here categorised in qualitative and quantitative. Qualitative results are based on direct observations on the acquired data, focusing on the distribution of the corrosion products. Quantitative results are based on the post-processing procedures detailed above such as phase segmentation. Quantitative observations include the corrosion level of the reinforcing bar, the composition of the sample, the thickness of the porous layer and corrosion products surrounding the reinforcing bar and the expansion coefficient of the corrosion products.

3.1. Qualitative observations

3.1.1. Corrosion distribution in natural and artificially corroded samples

Fig. 9 shows the distribution of the corrosion products over the length of the bar in the naturally (left) and artificially corroded sample (right), as obtained from the segmentation procedure described in Section 2.3.4. The naturally corroded sample appears almost not corroded, except for two large, visible pits. Those pits are located in correspondence of macro-pores (see Fig. 10). The artificially corroded sample shows, instead, a fairly uniform distribution of the corrosion products along the surface of the bar. Corrosion is also observed to adhere to the surface of macroscopic interfacial pores, and smaller corrosion particles appear to have migrated through the sample.

Corrosion products appear to have a substantially different distribution in the two samples. This is to be expected, given the differences in exposure and corrosion process of the two samples. In particular, the presence of chlorides in the concrete mixture for the artificially corroded sample, the use of induced current, and the casting procedure, where the bar was hold vertical, are likely to result in uniformly distributed corrosion products over the entire length of the bar [50]. This, to the

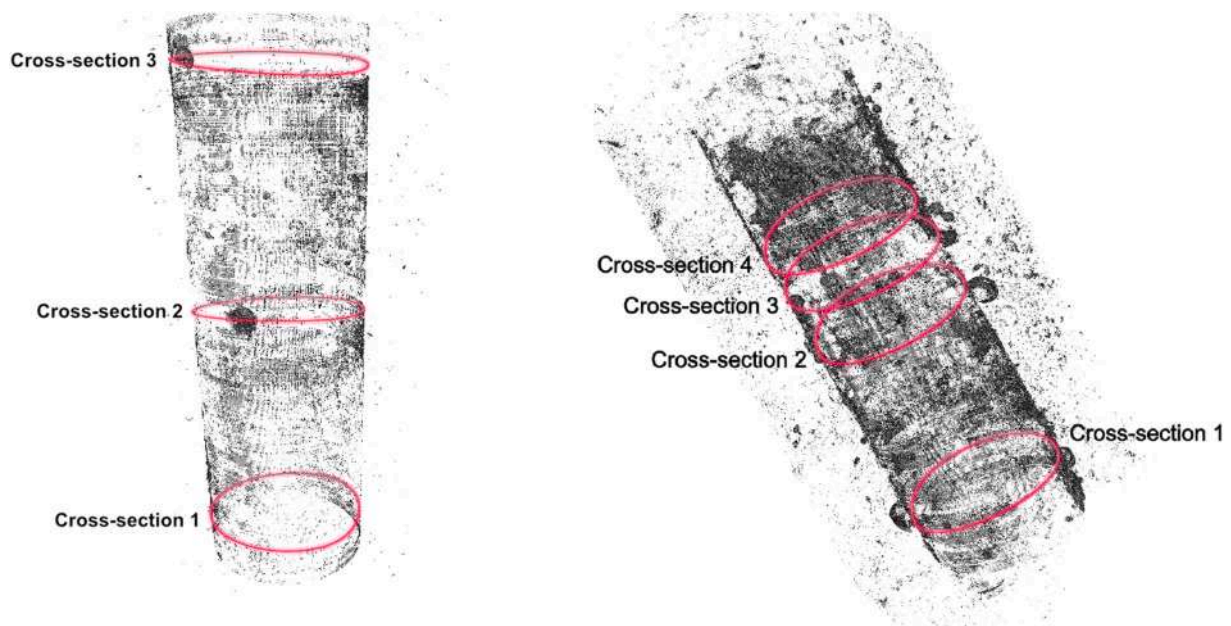


Fig. 9. 3D rendering of the corrosion distribution around the bar for the naturally corroded sample (left) and the artificially corroded sample (right). In red, the location of the cross-sectional views presented in Figs. 10 and 11 are shown. (For interpretation of the references to colour in this figure legend, the reader is referred to the web version of this article.)

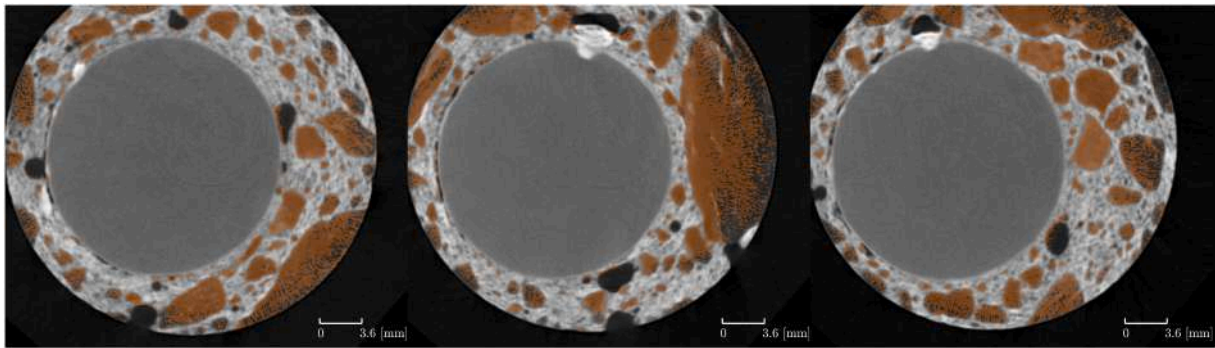


Fig. 10. Horizontal slices of the naturally corroded sample, view of three different pits. From left to right: cross-sections 1, 2 and 3, see Fig. 9. Aggregates are highlighted in orange using complementary X-ray data.

authors' knowledge, was however here observed for the first time using neutron imaging. Similar observations were reported in recent studies using X-ray computed tomography [51,36,52]. Corrosion in naturally corroded specimens, instead, initiates at the bar surface where the passive film locally breaks down, as a result of an inhomogeneity in the passive film, or in the chloride ingress. Corrosion products are therefore expected to be confined to isolated areas, in the form of pitting corrosion.

Additionally, migration of corrosion products through the cement paste may be linked to the solubility of the corrosion products originated from the corrosion process. Malumbela et al. [45] argues that the practice of immersing the specimens in NaCl solutions together with the use of impressed current (as done for the artificially corroded sample in this study) prevents oxygen from diffusing into the concrete to reach the anode, by filling up pores with moisture. This, in turn, results in the formation of ferrous hydroxide ($Fe(OH)_2$). This product is more soluble

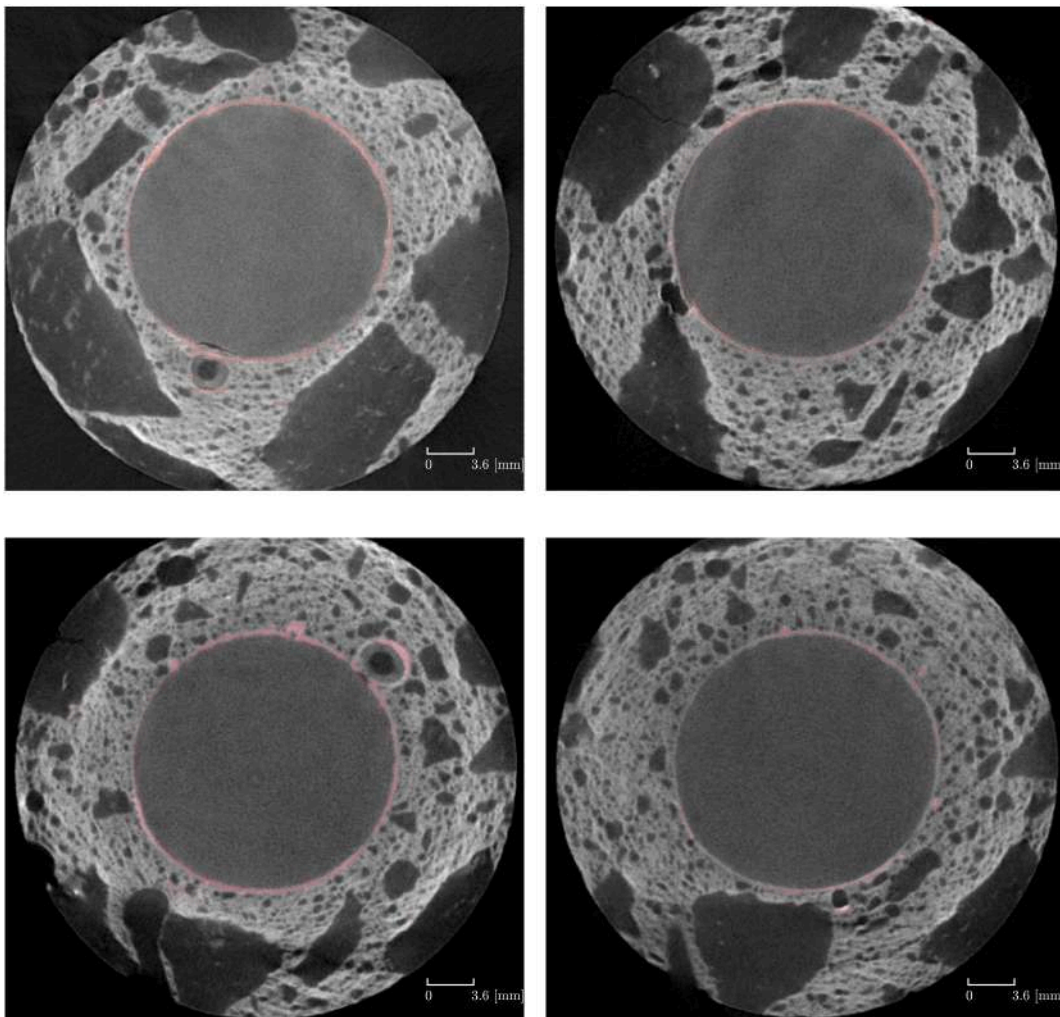


Fig. 11. Horizontal slices of the artificially corroded sample, highlighting the distribution of corrosion products (in red) in four different cross sections with pits. From left to right, top to bottom: cross sections 1, 2 3 and 4 in Fig. 9. (For interpretation of the references to colour in this figure legend, the reader is referred to the web version of this article.)

than other corrosion products with lower iron-to-rust ratios, such as magnetite (Fe_3O_4) or haematite ($\alpha - Fe_2O_3$), as highlighted in Table 1. Jaffer et al. [53] observed a dependency between the concrete porosity and the migration of corrosion products through the cement paste, where migration of the products would increase with the concrete porosity. High concrete porosity, and the formation of a more soluble corrosion product under accelerated corrosion conditions, may explain the spatial distribution of corrosion products in the artificially corroded sample shown in Fig. 9.

3.1.2. Corrosion in macroscopic interfacial concrete voids

Fig. 10 shows different types of macroscopic interfacial concrete voids in the naturally corroded sample. Corrosion products are represented in white, corresponding to higher neutron attenuation. In contrast, voids, having low attenuation coefficients, are shown as dark features in the image. The high contrast between the corrosion products and the pore, and the dry status of the sample at the time of scanning suggest the absence of pore solution.

In all cases, the presence of corrosion products is clearly linked to the presence of a macro-pore adjacent to the bar. However, the presence of a macro-pore does not necessarily result in the formation of corrosion products, as can be observed for example in Fig. 10 (left). Corrosion products are observed to partially occupy the pore, growing directly from the corresponding corrosion pit in the reinforcing bar.

Fig. 11 shows different interfacial macroscopic voids in the artificially corroded sample, highlighting how the bar is surrounded by an almost homogeneous layer of corrosion products. Corrosion products are highlighted in red, using complementary x-ray data. Corrosion products appear to adhere to the cement paste, instead of the bar. This is particularly evident for large pores, where corrosion products are observed to surround the pore perimeter, instead of growing from the pit as in the natural corroded case. A similar distribution was observed by Michel et al. [27], where corrosion products were observed to deposit at the mortar surface of artificially corroded specimens with a w/c ratio of 0.4 and 0.5, while for the case of a w/c ratio equal to 0.3, corrosion products were observed to adhere to the reinforcing bar.

In Fig. 11 (left), different layers of products can be observed in the pore itself, of which the outer one is similar to the other corrosion products, but the inner one contains lower amounts of hydrogen, with a corresponding attenuation coefficient falling in between that of the composition of the bar and the other corrosion products. Additionally, the presence of a pore is not necessarily linked to an increased presence of corrosion products in that region, i.e. corrosion products are rather uniformly distributed along the bar irrespective of neighbouring pores (Fig. 11, top, right).

Macroscopic interfacial concrete pores are expected to strongly affect the corrosion initiation phase. In particular, the degree of saturation is expected to have an impact on the corrosion distribution. In the

naturally corroded sample, corrosion products are observed in correspondence to the macroscopic interfacial pores: this behaviour is generally observed in saturated or partially saturated voids [11]. Additionally, in the naturally corroded sample, all observed pits share similar locations in the cross-section of the sample: this is most likely linked to the casting position of the reinforcing bar. Being the bar top-cast, a bleeding zone is likely to have formed underneath the bar [41,42]. Additionally, the casting method, which was by tamping, is likely to result in increased porosity of the concrete and size of the bleeding zone, compared to if the concrete was vibrated [54]. Note that in Fig. 10, the cross section of the bar is not oriented as on the bridge; the bleeding zone is most probably located at the left side of the figure. In the artificially corroded sample, pores do not show any systematic effect on the corrosion distribution.

3.1.3. Migration of corrosion products through cracks

While the naturally corroded sample was uncracked, the artificially corroded sample presented corrosion induced cracks. In Fig. 12, different cross-sectional views of the cracks are presented.

Corrosion products were clearly present in some cracks (Fig. 12, left and centre). Large corrosion stains were also observed on the surface of the sample before coring (see Fig. 4). However, it was not possible to observe the presence of corrosion products in all cracks (Fig. 12, right). The average crack width of the cracks, from left to right in figure, was estimated respectively equal to 0.11 mm, 0.16 mm and 0.07 mm. The width of the cracks seems to be of influence, and corrosion products seem to preferentially deposit in larger cracks.

It is interesting to observe that most cracks are able to propagate through the aggregates. This is rather uncommon for concrete of ordinary Portland cement (in the absence of alkali-silica/alkali-aggregates reactions), and may indicate either the presence of particularly weak aggregates, or of cement paste of comparable strength. Additionally, most of the observed cracks intersected a macroscopic interfacial pore. This can as well be connected to the observed behaviour. The presence of cracks intersecting macro-pores prevented a rigorous evaluation of the corrosion expansion coefficient in those pores: when attempted, the amount of corrosion products was shown to be equal or lower than the computed loss of steel, which is unreasonable given the chemical composition of the rust. This suggests that corrosion products have migrated through the cracks, and possibly reaching to the surface of the specimen, as corrosion stains were found on the sample surface in correspondence of cracks.

The penetration of corrosion products into cracks is still a highly debated topic [12], although it is generally accepted that migration of corrosion products is linked to the presence of a pressure gradient generated by the expanding corrosion products. Val et al. [55] studied migration of corrosion products through corrosion induced cracks, using samples with characteristics similar to the artificial one presented in this

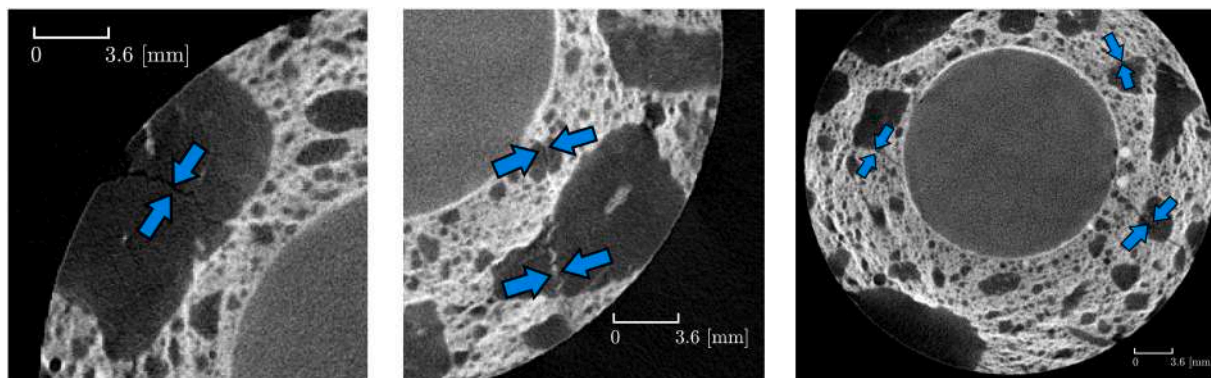


Fig. 12. Cross sectional views of the artificially corroded sample: corrosion products (in white), are observed to migrate towards the external surface of the sample (left and centre). However, not all cracks appear to be filled with corrosion products (right).

paper (artificially corroded, 3% CaCl_2 by weight of cement in the concrete mixture and partially submerged sample), and concluded that, generally, the amount of corrosion products flowing through the crack is overestimated when omitting time-dependency in the migration process, and assuming that the products start flowing from the instant the crack opens.

3.2. Quantification of the corrosion process

3.2.1. Composition of the samples

Fig. 13 shows the composition of the two samples, as identified from phase segmentation (as detailed in Section 2.3.4). The relative cumulative percentage of the phases is shown along the length of the bar, where different colours correspond to different material phases. It is important to note that the two samples had different material radii (the artificially corroded sample being larger), which justifies the difference in the volumetric fraction of bar in the two cases despite the similar sizes.

The total amount of corrosion products is shown to be relatively small in terms of volume fraction in both samples, particularly in the naturally corroded sample. The artificially corroded sample appears to contain a significant fraction of macroscopic voids.

The presence of local fluctuations likely caused by noise in the artificially corroded measurements is visible from the phase segmentation diagram (Fig. 13, right). As elaborated in Section 2.3.1, this was mostly attributed to the presence of NaCl in the cement paste and to the sample being partially wet at the time of scanning. Data from the naturally corroded sample, on the other hand, shows less pronounced local fluctuations.

3.2.2. Corrosion distribution

The corrosion level of the steel bars was evaluated by comparing the corroded area of the reinforcing bar to its estimated average area prior the corrosion process (see Section 2.3.7). Fig. 14 offers an overview of the corrosion level of the two reinforcing bars embedded in the samples. The average corrosion level of each section is plotted against the length of the bar, while the radius of the bar, with respect to its centre, is shown in a contour plot with the length of the bar and the rotation angle in the $x - y$ axis, resulting in a complete 2D view of the bar surface.

Differences in corrosion patterns between the two bars can be clearly observed: while the naturally corroded sample is characterised by two large corrosion pits at 33 and 55 mm around a $-\pi/2$ angle, alongside minor spots of corrosion, corrosion damages are almost uniformly distributed along the length of the artificially corroded bar. Note that the estimation of the corrosion level is more precise for the case of the artificially corroded sample, for which the original geometry of the embedded bar is known *a-priori*.

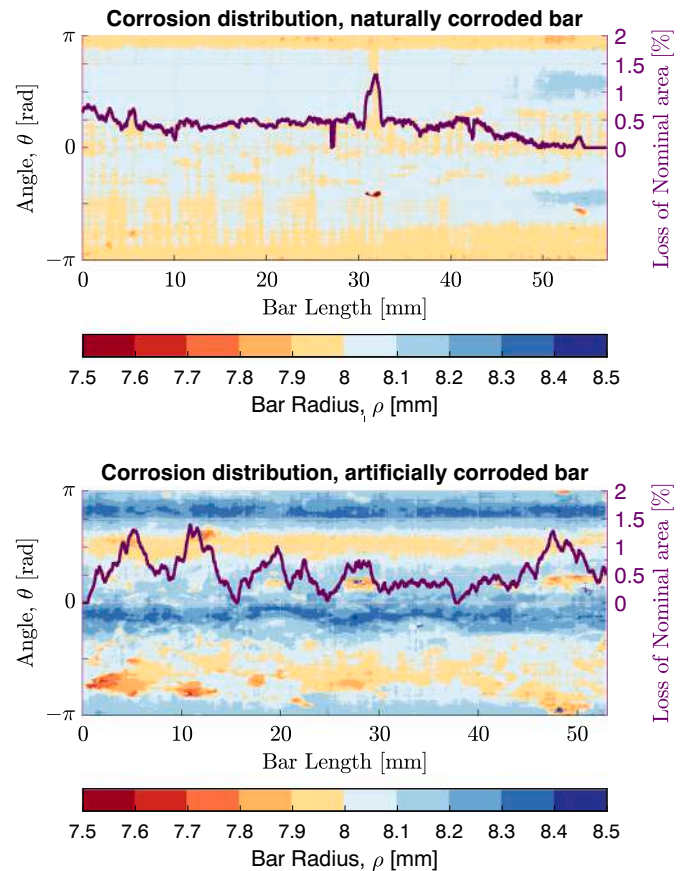


Fig. 14. Corrosion distribution along the length of naturally corroded bar (top) and artificially corroded bar (bottom). The loss of nominal area is represented by the continuous purple line, and refers to the right y-axis. (For interpretation of the references to colour in this figure legend, the reader is referred to the web version of this article.)

3.2.3. Thickness of the layer of voids and corrosion products surrounding the bar

In Figs. 15, 16, 17 and 18, the thickness of voids and corrosion products surrounding the bar is presented (whose evaluation is detailed in Section 2.3.5). Therein, the average thickness is presented along the length and across the perimeter of the bar for each specimen. Each measurement is the average of the maximum thicknesses of voids/corrosion products for a given portion of the specimen, thus, adding the

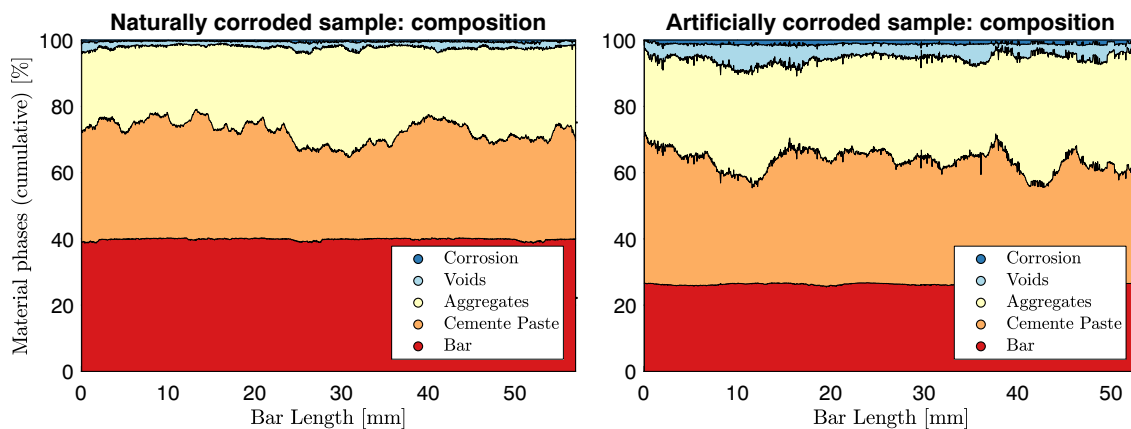


Fig. 13. Composition of the naturally corroded (left) and artificially corroded sample (right), after phase segmentation. Note that the artificially corroded sample had a larger diameter than the naturally corroded one, therefore the bar constitute a lower percentage of the sample composition.

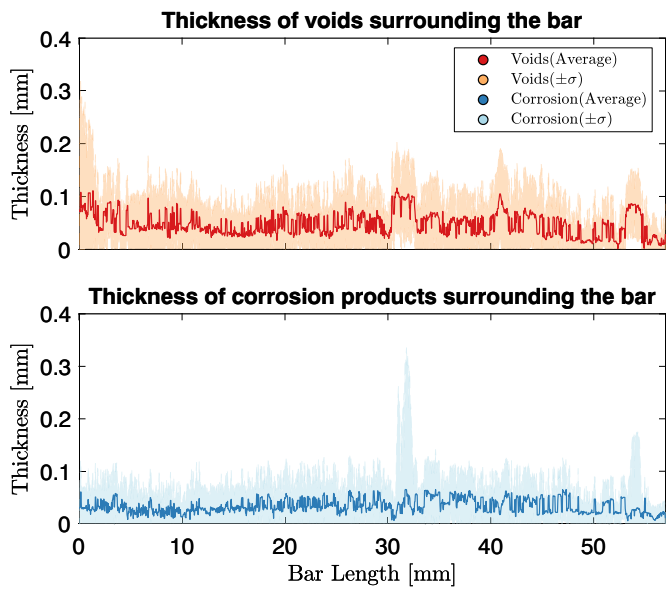


Fig. 15. Thickness of voids and corrosion products along the length of the bar in the naturally corroded sample.

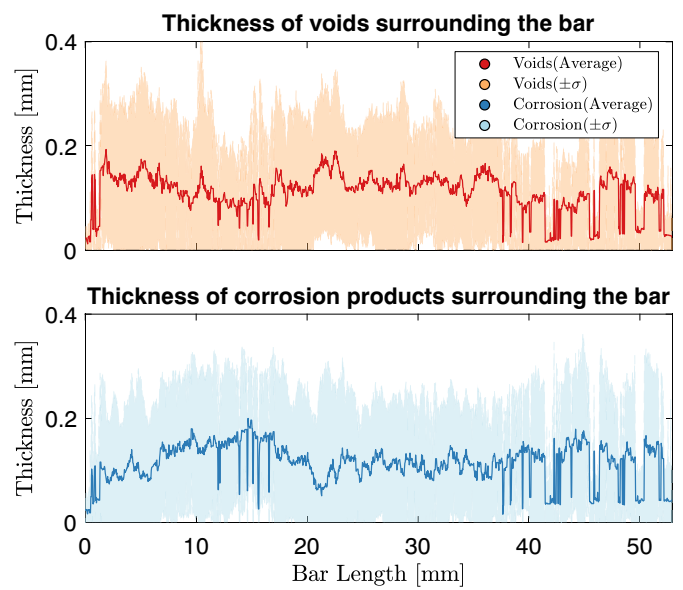


Fig. 17. Thickness of voids and corrosion products along the length of the bar in the artificially corroded sample.

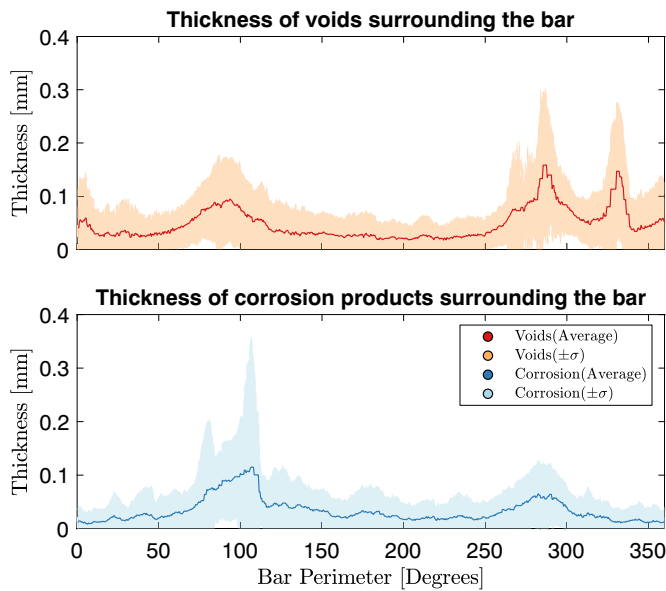


Fig. 16. Thickness of voids and corrosion products along the perimeter of the bar in the naturally corroded sample.

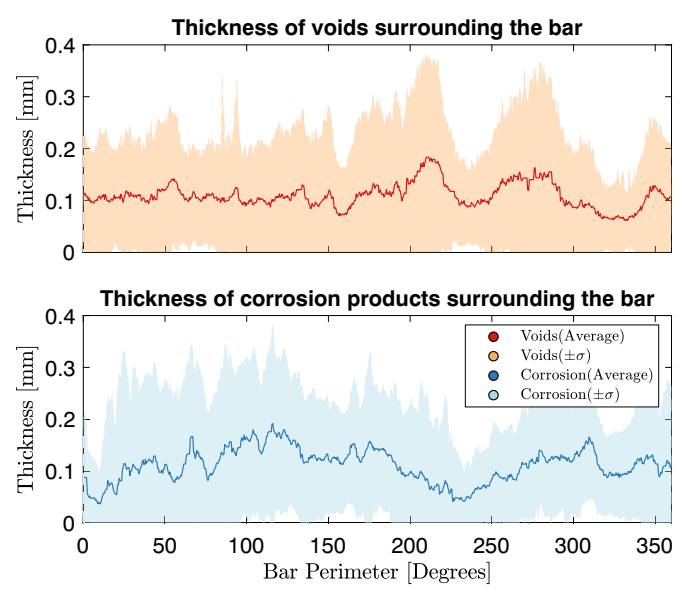


Fig. 18. Thickness of voids and corrosion products along the perimeter of the bar in the artificially corroded sample.

thickness of voids to the thickness of the corrosion products would lead to a large overestimation of the CAR. The error-band in the plots represents one standard deviation, as estimated locally, to highlight the spatial variation of this measure in the specimen.

In the naturally corroded sample (Figs. 15 and 16) voids and corrosion products predominantly appear in the same areas of the perimeter. This is likely linked to the top-cast position of the bar; those areas where both voids and corrosion products tend to accumulate around the bar are likely to indicate the position of the bleeding zone.

In the artificially corroded sample (Figs. 17 and 18), both voids and corrosion appear to be almost uniformly distributed along the steel concrete interface. The thickness of the corrosion products at the steel concrete interface can be observed to be on average around 100 μm , while the average thickness of voids appears to be between 100 and 200 μm . The thickness of the voids in the naturally corroded sample is

instead less than 100 μm , though localised macro-pores are significantly larger. It should nonetheless be noted that, the two samples are in two different stages of the corrosion process, where the naturally corroded sample shows only localised pitting corrosion, while in the artificially corroded sample the thickness of corrosion products at the steel concrete interface induces cracks in the surrounding concrete.

Experimental observations on specimens with corrosion induced cracks were carried out by Michel et al. [27]. They observed an increase with time of the thickness of the corrosion products surrounding the bar, up to the point of formation of corrosion induced cracks in the specimen. This can be explained by the increasing pressure on the concrete matrix induced by the corrosion products.

In this study, only one sample state was studied, which does not allow the study of the growth of the corrosion products thickness at the steel concrete interface over time. The proposed non-destructive approach allows nonetheless this time-resolved study.

3.2.4. Expansion coefficients of the corrosion product in macroscopic interfacial voids

The amount of corrosion products in macroscopic interfacial voids was quantified, and compared to the corresponding loss of steel in the corrosion pit to estimate the iron-to-rust volumetric ratio detailed in Section 2.3.6. The chosen macro-pores (see Fig. 8) were not completely filled with corrosion products, which could therefore be assumed to be free to expand. The results from the quantification of the iron-to-rust ratio in the macro-pores are summarised in Table 2.

The iron-to-rust volume ratio of the corrosion products is probably one of the most challenging parameters to estimate when describing the corrosion process of reinforced concrete structures. This is due to the nature of the corrosion products, which react with oxygen when exposed, and its dependency from exposure conditions, such as the moisture content of the pores.

The iron-to-rust volume ratios for the naturally corroded sample were estimated to be 4.24 and 4.13. The two values are reasonably close for the two analysed corrosion pits. This indicates similar composition of the corrosion products along the bar length. The results show that the ratios are on the higher end (around 4), with respect to the composition of corrosion products commonly assumed in corrosion models. This iron-to-rust volume likely corresponds to ferric hydroxide ($Fe(OH)_3$). This type of product is associated to high moisture levels, since an increase in oxygen supply is generally linked to the formation of more stable products, with smaller iron-to-rust volume ratios, such as haematite ($\alpha - Fe_2O_3$) and magnetite (Fe_3O_4) [45].

The estimated iron-to-rust ratio observed for the artificially corroded sample is slightly smaller than for the naturally corroded sample, and equal to 3.91. The ratio points in the direction of ferrous hydroxide ($Fe(OH)_2$), one of the most soluble corrosion products. Ferrous hydroxide generally forms in environments with high moisture content, and has been previously identified as a component of corrosion products in laboratory experiments, where corrosion was induced by using accelerated corrosion methods [45,23].

Additionally, the average iron-to-rust volumetric ratio was estimated for all the corrosion products present in the artificially corroded sample, to be around a value of 2.25. This volume ratio is lower than that calculated for the specific corrosion pit. This may result from a non-uniformity in the types of corrosion products present in the sample, but is more probably connected to the following factors:

1. Corrosion products, when at the interface between steel and concrete, are most likely compressed. The presence of corrosion induced cracks is a strong indicator of this being the case;
2. Corrosion products were observed to migrate through the corrosion induced cracks, and corrosion stains were found at the outside surface of the sample;
3. The presence of grains of NaCl introduced additional attenuation possibly increasing the total amount of corrosion products computed.

Given that the evaluated ratio is much smaller than that computed for the macropore, the first two uncertainties likely have a greater influence on the data.

Table 2

Iron to rust ratio in interfacial macroscopic pores and in the artificially corroded sample.

Corrosion pits	Iron to rust volumetric ratio
Naturally corroded sample, Pit 1	4.24
Naturally corroded sample, Pit 2	4.13
Artificially corroded sample, Pit 1	3.91
Artificially corroded sample, entire sample	2.25 ^a

^a Note that in this specific test, corrosion products were likely compressed at the steel/concrete interface, affecting this volume measurement.

It was not possible to make a similar estimation for the naturally corroded sample, where the absence of precise data on the original area of the bar, together with the particularly low amount of corrosion products, which were concentrated in specific locations along the length of the sample, yielded a non-physical value.

Finally, it is interesting to point out that the evaluated iron-to-rust ratios are higher than the coefficient generally used for the calibration of corrosion models. They are, however, reasonably within the range of the possible iron-to-rust ratios of iron oxides and hydroxides (see Table 1). Additionally, it is not uncommon for the values assumed in corrosion models to be calibrated *a posteriori* to fit the time of corrosion cracking observed in laboratory experiments. Since the time of cracking is influenced by many factors, this calibration method can be questionable.

4. Conclusions and outlook

In this work, two concrete samples with embedded reinforcement bars that have been subjected to different corrosion processes were studied using multimodal neutron and X-ray tomography. The aim of this work was to investigate the applicability of multimodal neutron and X-ray imaging for the non-destructive observation of corrosion processes. Additionally, this work proposes a number of image analysis methods to quantify key metrics, and suggests possible uses to further improve our knowledge of the corrosion process, particularly to be used in modelling of corrosion cracking.

The main findings are summarised below.

- Multimodal neutron and X-ray computed tomography is a promising non-destructive technique for qualitative and quantitative investigation of corrosion products in reinforced concrete samples. Though best results, *i.e.* ideal signal to noise ratios, are obtained when minimising the amount of strongly (neutron or X-ray) attenuating constituents that are not of interest to the experiment when preparing the sample, the technique can as well be used on samples extracted from real structures with good results.
- The corrosion distribution was observed to be substantially different between the naturally corroded and artificially corroded samples. In the naturally corroded sample, corrosion products were mostly present in interfacial macroscopic voids. In the artificially corroded sample, corrosion products were almost uniformly distributed along the length of the bar. Additionally, corrosion products were observed to adhere to the cement paste for the case of the artificially corroded sample, while adhering to the bar in the naturally corroded sample. This observation highlights the limitations of using the galvanostatic method for predicting the mechanical response of reinforced concrete structures affected by corrosion damages, especially in those situations where pitting corrosion constitutes the major risk for structural safety.
- Key metrics for the modelling of the corrosion process were observed, particularly it was possible to measure the thickness of the corrosion products at the steel concrete interface, the iron-to-rust ratio, and observe the distribution of corrosion products with respect to the presence of macro-pores.

Additionally, the following observations were made with respect to the analysed samples:

- Corrosion products were observed to migrate through some of the corrosion induced cracks in the artificially corroded sample.
- In the naturally corroded sample, the systematic presence of larger voids on one side of the bar (which was identified as the bleeding zone resulting from the top-cast position of the analysed bar) was linked to increasing presence of corrosion products in that zone.
- The iron-to-rust volumetric ratio quantified from the tomographies was between 4.13 and 4.24 for the naturally corroded sample, and

3.91 for the artificially corroded sample. These ratios are typical for corrosion products forming in saturated and partially saturated zones, such as ferrous and ferric hydroxide. These findings contradict the lower ratios, corresponding to corrosion products forming in environments with larger availability of oxygen, commonly assumed in corrosion models.

Funding

This project was supported by funding provided by Swedish Research Council Formas grant 2016-00568 and Swedish Transport Administration grant TRV 2017/39084.

CRedit authorship contribution statement

Samanta Robuschi: Investigation, Conceptualization, Software, Visualization, Writing - Original draft
Alessandro Tengattini: Investigation, Supervision, Writing - Review & editing
Jelke Dijkstra: Conceptualization, Supervision Writing - Review & editing, Funding acquisition
Ignasi Fernandez: Supervision, Writing - Review & editing
Karin Lundgren: Conceptualization, Supervision, Writing - Review & editing, Funding acquisition.

Declaration of competing interest

The authors declare that they have no known competing financial interests or personal relationships that could have appeared to influence the work reported in this paper.

Acknowledgements

The authors would like to acknowledge the ILL for granting the possibility to carry on the experimental work at the D50T instrument (research proposal UGA-57 and UGA-78). The data used in this work are made available at <https://doi.org/10.5291/ILL-DATA.UGA-57> and <https://doi.org/10.5291/ILL-DATA.UGA-78>. Additionally, the computations were enabled by resources provided by the Swedish National Infrastructure for Computing (SNIC) at Chalmers Centre for Computational Science and Engineering (C3SE) partially funded by the Swedish Research Council through grant agreement no. 2018-05973.

Appendix A

In this section, the steps of the multimodal correlation algorithm are presented in details. It is to be noted that this algorithm is tailored to the specific geometrical characteristics of the data acquired in this work, *i.e.* the cylindrical shape of the concrete sample, and the presence of a plain bar embedded in the sample, that can as well be approximated to a cylindrical shape.

1. A cylinder is fitted to the acquired neutron and X-ray data. The average radius, and the centre line are computed for both data sets;
2. The neutron imaging data are downscaled to the X-ray data resolutions. The rescaling process is based on the ratio between the average radius of the cylindrical approximations and uses a bi-cubical approximation;
3. The rescaled neutron data set is aligned along the z direction with the X-ray data set. This is done by thresholding the data, so that the background is separated from the concrete sample. The area of the sample is then calculated for each image of the data set. Alignment is obtained by iteratively minimising the difference in area between corresponding horizontal slices of the sample.
4. The neutron imaging data are translated in the x and y direction (*i.e.*, in the cross sectional view plane), so that the average centre of the

horizontal slices would correspond in both modalities. The translation matrix is evaluated by assuming the sample to be perfectly cylindrical.

5. A rotation angle is then computed, to be applied in the $x - y$ plane. The rotation angle is obtained by overlapping the two data sets and iteratively minimising the area of the resulting figure. The presence of voids in the external perimeter of both samples ensures a proper alignment. However, this procedure assumes the data sets to be already aligned in the $x - z$ and $x - y$ plane, as a result of the acquisition procedure. The error introduced by this assumption was assumed to be negligible through visual observation.
6. The neutron data set is then rotated of the angle resulting from the previous step in the $x - y$ plane using a bi-cubical approximation.

References

- [1] B. Bell, European Railway Bridge Demography - Deliverable D 1.2, Tech. Rep. (2004).
- [2] K. Lundgren, Effect of corrosion on the bond between steel and concrete: an overview, *Mag. Concr. Res.* 59 (6) (2007) 447–461, <https://doi.org/10.1680/mac.2007.59.6.447>.
- [3] I. Fernandez, C.G. Berrocal, Mechanical properties of 30 year-old naturally corroded steel reinforcing bars, *International Journal of Concrete Structures and Materials* 13 (1) (2019), <https://doi.org/10.1186/s40069-018-0308-x>.
- [4] R. François, I. Khan, V.H. Dang, Impact of corrosion on mechanical properties of steel embedded in 27-year-old corroded reinforced concrete beams, *Mater. Struct.* 46 (6) (2013) 899–910, <https://doi.org/10.1617/s11527-012-9941-z>.
- [5] M. Tahershamsi, K. Zandi, K. Lundgren, M. Plos, Anchorage of naturally corroded bars in reinforced concrete structures, *Mag. Concr. Res.* 66 (14) (2014) 729–744, <https://doi.org/10.1680/mac.13.00276>.
- [6] I. Fernandez, M. F. Herrador, A. R. Marí, J. M. Bairán, Ultimate capacity of corroded statically indeterminate reinforced concrete members, *International Journal of Concrete Structures and Materials* v(1) (Dec 2018). doi:<https://doi.org/10.1186/s40069-018-0297-9>.
- [7] M.M. Kioumarsis, M.A.N. Hendriks, J. Kohler, M.R. Geiker, The effect of interference of corrosion pits on the failure probability of a reinforced concrete beam, *Engineering Structures* 114 (2016) 113–121, <https://doi.org/10.1016/j.engstruct.2016.01.058>.
- [8] J. Zhang, X. Ling, Z. Guan, Finite element modeling of concrete cover crack propagation due to non-uniform corrosion of reinforcement, *Construction and Building Materials* 132 (2017) 487–499, <https://doi.org/10.1016/j.conbuildmat.2016.12.019>.
- [9] K. Zandi Hanjari, K. Lundgren, M. Plos, D. Coronelli, Three-dimensional modelling of structural effects of corroding steel reinforcement in concrete, *Struct. Infrastruct. Eng.* 9 (7) (2013) 702–718, <https://doi.org/10.1080/15732479.2011.607830>.
- [10] X. Xi, S. Yang, C.Q. Li, A non-uniform corrosion model and meso-scale fracture modelling of concrete, *Cement and Concrete Research* 108 (March) (2018) 87–102, <https://doi.org/10.1016/j.cemconres.2018.03.009>.
- [11] U.M. Angst, M.R. Geiker, M.C. Alonso, R. Polder, O.B. Isgor, B. Elsener, H. Wong, A. Michel, K. Hornbostel, C. Gehlen, R. François, M. Sanchez, M. Criado, H. Sørensen, C. Hansson, R. Pillai, S. Mundra, J. Gulikers, M. Raupach, J. Pacheco, A. Sagués, The effect of the steel–concrete interface on chloride-induced corrosion initiation in concrete: a critical review by RILEM TC 262-SCL, *Mater. Struct.* 52 (4) (2019), <https://doi.org/10.1617/s11527-019-1387-0>.
- [12] K.G. Papakonstantinou, M. Shinozuka, Probabilistic model for steel corrosion in reinforced concrete structures of large dimensions considering crack effects, *Engineering Structures* 57 (2013) 306–326, <https://doi.org/10.1016/j.engstruct.2013.06.038>.
- [13] D. R. Lide, CRC Handbook of Chemistry and Physics., Internet Version Edition, Boca Raton, FL, 2005. doi:<https://doi.org/10.5860/choice.41-4368>. URL <http://www.hbcpnetbase.com>.
- [14] K. Tuutti, Corrosion of Steel in Concrete, Tech. Rep., Swedish Cement and Concrete Research Institute, Stockholm, 1982. URL, <https://lucris.lub.lu.se/ws/cems/4709458/3173290.pdf>.
- [15] F.J. Molina, C. Andrade, Cover cracking as a function of rebar corrosion: part 2—numerical model, *Mater. Struct.* 26 (9) (1993) 532–548, <https://doi.org/10.1007/BF02472864>.
- [16] K. Bhargava, A. Ghosh, Y. Mori, S. Ramanujam, Analytical model for time to cover cracking in RC structures due to rebar corrosion, *Nucl. Eng. Des.* 236 (11) (2006) 1123–1139, <https://doi.org/10.1016/j.nucengdes.2005.10.011>. URL, <https://linkinghub.elsevier.com/retrieve/pii/S0029549305003833>.
- [17] K. Lundgren, Modelling the effect of corrosion on bond in reinforced concrete, *Magazine of Concrete Research* 54 (3) (2002) 165–173. URL <http://www.icevirtuallibrary.com/content/journals>.
- [18] Y. Zhao, H. Ren, H. Dai, W. Jin, Composition and expansion coefficient of rust based on X-ray diffraction and thermal analysis, *Corrosion Science* 53 (5) (2011) 1646–1658, <https://doi.org/10.1016/j.corsci.2011.01.007>.
- [19] S. Syed, *Corros. Sci.* 50 (6) (2008) 1779–1784, <https://doi.org/10.1016/J.CORSCI.2008.04.004>. URL, <https://www.sciencedirect.com/science/article/pii/S0010938X08001303?via>.

- [20] S. Williamson, L.A. Clark, Effect of corrosion and load on reinforcement bond strength, *Struct. Eng. Int.* (2002) 113–119, [https://doi.org/10.1130/0091-7613\(1977\)5<429:ARFR>2.0.CO;2](https://doi.org/10.1130/0091-7613(1977)5<429:ARFR>2.0.CO;2).
- [21] T.D. Marcotte, *Characterization of Chloride-induced Corrosion Products that Form in Steel-reinforced Cementitious Materials*, University of Waterloo, 2001.
- [22] F. Chen, H. Baji, C.Q. Li, A comparative study on factors affecting time to cover cracking as a service life indicator, *Construction and Building Materials* 163 (2018) 681–694, <https://doi.org/10.1016/j.conbuildmat.2017.12.120>.
- [23] A. Michel, B.J. Pease, M.R. Geiker, H. Stang, J.F. Olesen, Monitoring reinforcement corrosion and corrosion-induced cracking using non-destructive x-ray attenuation measurements, *Cem. Concr. Res.* 41 (11) (2011) 1085–1094, <https://doi.org/10.1016/j.cemconres.2011.06.006>. URL, <https://www.sciencedirect.com/science/article/pii/S0008884611001670>.
- [24] I. Petre-Lazar, Evaluation du comportement en service des ouvrages en béton armé soumis à la corrosion des aciers - Outil d'aide à la décision, URL, Université Laval, 2000. [http://oatd.org/oatd/record?record=oai\(%5C%\)3Acollectionscanada.gc.ca\(%5C%\)3A00AMICUS.27590214](http://oatd.org/oatd/record?record=oai(%5C%)3Acollectionscanada.gc.ca(%5C%)3A00AMICUS.27590214).
- [25] Y. Liu, R.E. Weyers, Modeling the time-to-corrosion cracking in chloride contaminated reinforced concrete structures, *ACI Materials Journal* 95 (6) (1998) 675–680, <https://doi.org/10.14359/410>. URL, <http://www.concrete.org/Publications/ACIMaterialsJournal/ACIJSearch.aspx?m=detailsID=410>.
- [26] A. Jamali, U. Angst, B. Adey, B. Elsener, Modeling of corrosion-induced concrete cover cracking: a critical analysis, *Construction and Building Materials* 42 (2013) 225–237, <https://doi.org/10.1016/j.conbuildmat.2013.01.019>.
- [27] A. Michel, B.J. Pease, A. Peterová, M.R. Geiker, H. Stang, A.E.A. Thybo, Penetration of corrosion products and corrosion-induced cracking in reinforced cementitious materials: experimental investigations and numerical simulations, *Cement and Concrete Composites* 47 (2014) 75–86, <https://doi.org/10.1016/j.cemconcomp.2013.04.011>.
- [28] H.S. Wong, Y.X. Zhao, A.R. Karimi, N.R. Buenfeld, W.L. Jin, On the penetration of corrosion products from reinforcing steel into concrete due to chloride-induced corrosion, *Corrosion Science* 52 (7) (2010) 2469–2480, <https://doi.org/10.1016/j.corsci.2010.03.025>.
- [29] C. Fahy, S.J. Wheeler, D. Gallipoli, P. Grassl, Corrosion induced cracking modelled by a coupled transport-structural approach, *Cement and Concrete Research* 94 (2017) 24–35, <https://doi.org/10.1016/j.cemconres.2017.01.007>.
- [30] O. Stamati, E. Roubin, E. Andò, Y. Malecot, Phase segmentation of concrete x-ray tomographic images at meso-scale: validation with neutron tomography, *Cem. Concr. Compos.* 88 (2018) 8–16, <https://doi.org/10.1016/j.cemconcomp.2017.12.011>.
- [31] E. Roubin, E. Andò, S. Roux, The colours of concrete as seen by X-rays and neutrons, *Cement and Concrete Composites* 104 (December 2018) (2019), 103336, <https://doi.org/10.1016/j.cemconcomp.2019.103336>.
- [32] E. Tudisco, C. Jailin, A. Mendoza, A. Tengattini, E. Andò, S.A. Hall, G. Viggiani, F. Hild, S. Roux, An extension of digital volume correlation for multimodality image registration, *Meas. Sci. Technol.* 28 (9) (2017), <https://doi.org/10.1088/1361-6501/aa7b48>.
- [33] D. Dauti, A. Tengattini, S. Dal Pont, N. Toropovs, M. Briffaut, B. Weber, Analysis of moisture migration in concrete at high temperature through in-situ neutron tomography, *Cem. Concr. Res.* 111 (February) (2018) 41–55, <https://doi.org/10.1016/j.cemconres.2018.06.010>.
- [34] D. Dauti, A. Tengattini, S.D. Pont, N. Toropovs, M. Briffaut, B. Weber, Some observations on testing conditions of high-temperature experiments on concrete: an insight from neutron tomography, *Transport in Porous Media* (2020), 0123456789, <https://doi.org/10.1007/s11242-020-01392-2>.
- [35] P. Zhang, Z. Liu, Y. Wang, J. Yang, S. Han, T. Zhao, 3D neutron tomography of steel reinforcement corrosion in cement-based composites, *Construction and Building Materials* 162 (December 2017) (2018) 561–565, <https://doi.org/10.1016/j.conbuildmat.2017.12.057>.
- [36] B. Šavija, M. Luković, S.A.S. Hosseini, J. Pacheco, E. Schlangen, Corrosion induced cover cracking studied by X-ray computed tomography, nanoindentation, and energy dispersive X-ray spectrometry (EDS), *Mater. Struct.* 48 (7) (2015) 2043–2062, <https://doi.org/10.1617/s11527-014-0292-9>.
- [37] E. Rossi, R. Polder, O. Copuroglu, T. Nijland, B. Šavija, The influence of defects at the steel/concrete interface for chloride-induced pitting corrosion of naturally-deteriorated 20-years-old specimens studied through X-ray computed tomography, *Construction and Building Materials* 235 (2020), 117474, <https://doi.org/10.1016/j.conbuildmat.2019.117474>.
- [38] A. Tengattini, N. Lenoir, E. Andò, B. Giroud, D. Atkins, J. Beaucour, G. Viggiani, Next-grenoble, the neutron and x-ray tomograph in grenoble, *Nuclear Instruments and Methods in Physics Research Section A: Accelerators, Spectrometers, Detectors and Associated Equipment*, 2020, p. 163939.
- [39] S. Robuschi, K. Lundgren, I. Fernandez, M. Flansbjerg, Anchorage of naturally corroded plain reinforcement bars in flexural members, *Mater. Struct.* (2020) 1–26, <https://doi.org/10.1617/s11527-020-01471-2>.
- [40] S. Robuschi, J. Sumearl, I. Fernandez, K. Lundgren, Bond of naturally corroded, plain reinforcing bars in concrete, *Struct. Infrastruct. Eng.* (2020) 1–26.
- [41] U.M. Angst, M.R. Geiker, A. Michel, C. Gehlen, H. Wong, O.B. Isgor, B. Elsener, C. M. Hansson, R. François, K. Hornbostel, R. Polder, M.C. Alonso, M. Sanchez, M. J. Correia, M. Criado, A. Sagüés, N. Buenfeld, The steel–concrete interface, *Mater. Struct.* 50 (2) (2017) 143, <https://doi.org/10.1617/s11527-017-1010-1>.
- [42] R. Zhang, A. Castel, R. François, Influence of steel-concrete interface defects owing to the top-bar effect on the chloride-induced corrosion of reinforcement, *Mag. Concr. Res.* 63 (10) (2011) 773–781, <https://doi.org/10.1680/macr.2011.63.10.773>.
- [43] Swedish Standards Institute, SS-EN 197-1:2011 (2011).
- [44] C.G. Berrocal, I. Fernandez, K. Lundgren, I. Löfgren, Corrosion-induced cracking and bond behaviour of corroded reinforcement bars in SFRC, *Compos. Part B* 113 (2017) 123–137, <https://doi.org/10.1016/j.compositesb.2017.01.020>.
- [45] G. Malumbela, P. Moyo, M. Alexander, A step towards standardising accelerated corrosion tests on laboratory reinforced concrete specimens, *J. South Afr. Inst. Civil Eng.* 54 (2) (2012) 78–85.
- [46] MATLAB, Version R2017b, The MathWorks Inc., Natick, Massachusetts, 2017.
- [47] J. Schindelin, I. Arganda-Carreras, E. Frise, V. Kaynig, M. Longair, T. Pietzsch, S. Preibisch, C. Rueden, S. Saalfeld, B. Schmid, J.-Y. Tinevez, D.J. White, V. Hartenstein, K. Eliceiri, P. Tomancak, A. Cardona, Fiji: an open-source platform for biological-image analysis, *Nat. Methods* 9 (7) (2012) 676–682, <https://doi.org/10.1038/nmeth.2019>. URL, <http://www.nature.com/articles/nmeth.2019>.
- [48] C.A. Schneider, W.S. Rasband, K.W. Eliceiri, NIH Image to ImageJ: 25 years of image analysis, *Nat. Methods* 9 (7) (2012) 671–675, <https://doi.org/10.1038/nmeth.2089>. URL, <http://www.nature.com/articles/nmeth.2089>.
- [49] N. Otsu, A threshold selection method from gray-level histograms, *IEEE Trans. Syst. Man Cybern.* 9 (1) (1979) 62–66.
- [50] A. Poursae, C.M. Hansson, Potential pitfalls in assessing chloride-induced corrosion of steel in concrete, *Cement and Concrete Research* 39 (5) (2009) 391–400, <https://doi.org/10.1016/j.cemconres.2009.01.015>.
- [51] B. Dong, G. Shi, P. Dong, W. Ding, X. Teng, S. Qin, Y. Liu, F. Xing, S. Hong, Visualized tracing of rebar corrosion evolution in concrete with x-ray micro-computed tomography method, *Cement and Concrete Composites* 92 (September 2017) (2018) 102–109, <https://doi.org/10.1016/j.cemconcomp.2018.06.003>.
- [52] S. Hong, F. Zheng, G. Shi, B. Dong, M. Liu, L. Tang, Y. Zhang, Determining influence of impressed current density on current efficiency with X-ray micro-computed tomography, *Construction and Building Materials* 246 (2020), 118505, <https://doi.org/10.1016/j.conbuildmat.2020.118505>.
- [53] S.J. Jaffer, C.M. Hansson, Chloride-induced corrosion products of steel in cracked-concrete subjected to different loading conditions, *Cement and Concrete Research* 39 (2) (2009) 116–125, <https://doi.org/10.1016/j.cemconres.2008.11.001>.
- [54] K. J., S. H., Tranebergsbron i stockholm. provning och bedömning av vidhäftningen för släta armeringsstänger., *Teknisk rapport* 15 (1998) 1–27.
- [55] D.V. Val, L. Chernin, M.G. Stewart, Experimental and numerical investigation of corrosion-induced cover cracking in reinforced concrete structures, *Journal of Structural Engineering* 135 (4) (2009) 376–385, [https://doi.org/10.1061/\(ASCE\)0733-9445\(2009\)135:4\(376\)](https://doi.org/10.1061/(ASCE)0733-9445(2009)135:4(376)).